A Joint Data- and Model-Driven Approach Simulating the Behaviour of a Walkalong Glider

Dieuwertje Alblas[1], Mark van den Bosch[2], Lucas Jansen Klomp[3], Vivi Rottschäfer[4], Len Spek[5], Felix Schwenninger[6], Lotte Weedage[7] and Sjanne Zeijlemaker[8]

Abstract

Properly flying a walkalong glider is a challenging control problem, involving many internal and external influences. We have shed some light on this problem from both a model-driven and data-driven viewpoint. We construct a mathematical model, based on well-established models from literature. This model is used to derive an optimal paddle angle, as well as an optimal distance between the paddle and the glider for steady level flight. Moreover, we derive parameters of the glider during uniform circular flight, as well as their relation to movement of the paddle from our model. As the glider is in practice very sensitive to small

[1]University of Twente, The Netherlands
[2]Leiden University, The Netherlands
[3]University of Twente, The Netherlands
[4]Leiden University, The Netherlands
[5]University of Twente, The Netherlands
[6]University of Twente, The Netherlands
[7]University of Twente, The Netherlands
[8]Eindhoven University, The Netherlands

disturbances in the airflow, we have developed a data-driven model that tracks the status of the glider using video data, recorded by a camera mounted on the paddle. We use image processing and deep learning to automatically detect glider position with respect to the paddle and its yaw. Information from mathematical and data-driven models could be jointly used as an input for a control algorithm on the paddle, allowing for automatic operation of the walkalong glider.

KEYWORDS: walkalong glider, plane, flight dynamics, image analysis, control problem

5.1 Introduction

The artist Zoro Feigl works on a new art project in which a small glider flies on the wake of a moving board, controlled by a robot arm. The project is based on an idea of Joseph E. Grant in 1955, called the *walkalong glider* Grant (1955). This walkalong glider is controlled by a board, called the *paddle* (Figure 5.1). The glider flies on the airwave

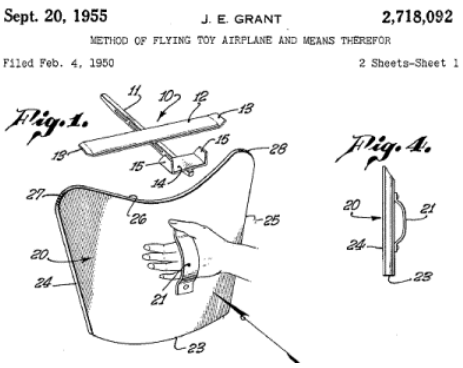

Figure 5.1: Sketch of the walkalong glider idea by Grant (1955).

that is caused by movement of the paddle, and by adjusting the angle of the paddle, the glider's trajectory can be influenced. See Feigl (2021) for a video clip of a walkalong glider demonstration.

5.1.1 Robot arm

The glider in the art project will be controlled by a robot arm with a transparent board mounted on its tip. The model that will be used is the FANUC M-710iC/12L, shown in Figure 5.2. This robot has six axes, which allows for a large range of motion. Figure 5.3 shows its length when fully extended (3.123 meters) and a side view of its reach. The flight path of the glider should always stay within this range. Additionally, we must stay above ground level, as the robot arm will be mounted to the floor. The wrist of the arm can move along three axes: the 'hand' can bend with respect to the arm and the wrist and tip (where the board is mounted) can be rotated 400 and 720 degrees respectively. This allows us to adjust the position and angle of the board relative to the glider.

Figure 5.2: The FANUC M-710iC/12L robot arm which is planned to be used to control the glider FANUC Benelux BV (2022).

An important restriction of this robot arm is that it can only rotate up to 360 degrees around its center. Hence, we cannot create a circular flight path by spinning the arm indefinitely.

5.1.2 Goal

The objective of this project is to explore how control on the glider's trajectory can be automated. Instead of a human operating the paddle, it is mounted on a robot arm that should autonomously keep the glider

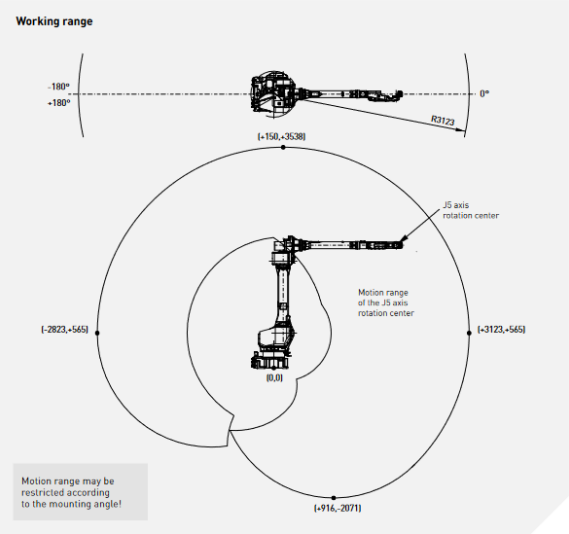

Figure 5.3: Range of motion of the FANUC M-710iC/12L robot arm FANUC Benelux BV (2022, datasheet).

in the air. This objective requires a control strategy for the robot arm that keeps the glider in the air, even under perturbations in the airflow (such as movement of observers). As a first step towards this objective, we investigated how to model the glider, which data is required to control the glider, and how this data should be processed.

5.1.3 Approach

We have split up this problem into two parts: a model-driven and a data-driven part. These two approaches both focus on a different aspect of the total control strategy: based on the model, we should be able to determine a global flight-path and predict where the glider will be at each moment in time. Additionally, we use a data-driven approach to make small corrections to the flight path and account for disturbances caused by external influences.

This report is set up as follows: first, we give an overview of im-

portant models from literature in Section 5.2, and investigate the effect of the paddle on the glider. Subsequently, in Section 5.3, we show the behaviour of the glider based on data analysis and show some key variables that are important to control in order to be able to keep the glider flying. We end this report with some recommendations and an outlook for further research in Section 5.4.

5.2 Model-driven approach

In this section, we consider two different approaches to calculate the flight path of the glider. Firstly, we study a more elaborate model, representing the glider by a point mass. First we introduce this model in a setting with no wind and then extend it to a scenario where wind is present. Subsequently, we simplify this model to approximate the glider angle and turning radius. This is explained in Section 5.2.3.

Both versions of the model rely on characteristics of the glider, as well as known equations from the literature. We begin this section with an overview of all parameters involved.

5.2.1 Definitions and formulas

Our models use several well-known formulas and physical constants from the literature. In this section, we give a brief overview. For a more detailed description, we refer to Stengel (2004, Chapter 1).

Table 5.1 gives a schematic overview of the symbols used in the glider model, their meaning and their value or formula. Some are known constants, such as the density of air at room temperature. However, most parameters depend on the particular glider that we use.

Our glider is based on the Baby Bug model from Harrison ScienceToyMaker (2022). It is made out of thin EMS foam with an aluminum weight at the nose. This glider has a total wing span of 20cm and a surface area of 12.2cm^2. Figure 5.4 shows the layout of a single wing; its mass is 0.147g.

Some other parameters from Table 5.1 depend on the characteristics of the glider, and cannot be measured directly; for example the Oswald efficiency number and drag coefficient at zero lift. For these parameters,

Symbol	Description	Value/formula
D	Drag force	$\frac{1}{2}C_D\rho V^2 S$
L	Lift force	$\frac{1}{2}C_L\rho V^2 S$
C_L	Lift coefficient	$C_{L_\alpha}\alpha$
C_{L_α}	Lift-slope derivative	$\frac{\pi AR}{1+\sqrt{1+(AR/2)^2}}$
C_D	Drag coefficient	$C_{D_0} + \varepsilon C_L^2$
C_{D_0}	Drag coefficient at zero lift	0.02
ϵ	Induced-drag factor	$1/(\pi ARe)$
AR	Aspect ratio	b^2/S
e	Oswald efficiency number	0.9
m	Mass of the glider	$1.47 \cdot 10^{-4}$kg
g	Gravitational acceleration	9.807 m/s^2
S	Surface area of the glider	0.0122m^2
ρ	Density of air	1.225 kg/m^3
b	Total wing span of the glider	0.2m
V	Relative air speed	See Section 5.2.2
α	Angle of attack	

Table 5.1: A description and its corresponding formula or value of the symbols used in the models.

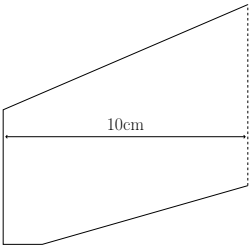

Figure 5.4: A left wing of the Baby Bug glider. The dashed line marks the center of the glider.

we used values for a similar paper airplane in Stengel (2004, Chapter 1).

5.2.2 Glider one point mass model

We first propose to model the glider as a one-point mass in space, similar to Etkin (2005) and Hull (2007). Figure 5.5 illustrates a free-body diagram of the forces acting on the centre of mass; note that the depiction of the glider is for illustrative purposes only.

The velocity of the glider relative to the ground ($\mathbf{U}$) will be written as the sum

$$\mathbf{U} = \mathbf{V} + \mathbf{W}, \tag{5.1}$$

with $\mathbf{V}$ the velocity of the airplane relative to the atmosphere and $\mathbf{W}$ the velocity of the atmosphere relative to the ground. Since the drag and lift are functions of the airspeed $V = \|\mathbf{V}\|$, decomposing the glider velocity $\mathbf{U}$ is more convenient. The lift and drag are respectively defined as:

$$L = \frac{1}{2}\rho V^2 S C_L \quad \text{and} \quad D = \frac{1}{2}\rho V^2 S C_D, \tag{5.2}$$

where the constants $C_L = C_L(\alpha)$ and $C_D = C_D(\alpha)$ depend on the angle of attack α. For our intents and purposes, we may assume there are no side forces acting on the glider. Differently put, the sideslip angle is assumed to be zero. For more information, we refer to Beeler, Moerder, and Cox (2003).

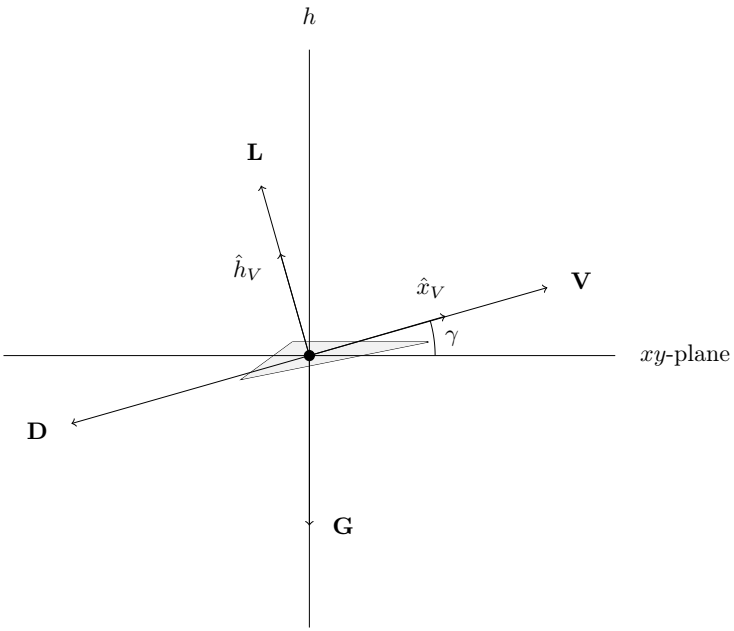

Figure 5.5: A free-body diagram of a glider with no ambient winds. The forces acting on the glider are assumed to be the lift force vector **L**, the drag force vector **D** and the gravity force vector $\mathbf{G} = (0, 0, -mg)^T$. The airspeed vector **V** is parallel to the vector **D** and perpendicular to the vector **L**, and $\hat{x}_V$ is defined to be the unit vector in the direction of **V**.

In this section, we will make use of the following two reference frames. Assuming a flat[9], non-rotating Earth, we obtain an inertial reference frame defined with axes aligned with the unit vector set

$$\hat{U}_I = \left(\begin{array}{c|c|c} & & \\ \hat{x} & \hat{y} & \hat{h} \\ & & \end{array} \right) = \left(\begin{array}{c|c|c} 1 & 0 & 0 \\ 0 & 1 & 0 \\ 0 & 0 & 1 \end{array} \right). \tag{5.3}$$

[9]The flat earth assumption suffices for our applications, but it is not necessary. See Etkin (2005) and Hull (2007) for flight models over a spherical Earth.

We refer to this inertial system as the "ground axes frame". A sequence of three simple rotations relates the inertial reference frame to a non-inertial, rotating reference frame whose axes are defined such that $\hat{U}_V = \begin{pmatrix} \hat{x}_V & \hat{y}_V & \hat{h}_V \end{pmatrix}$ with $\hat{x}_V = \mathbf{V}/V$. We call this the "wind axes frame"; in the absence of wind, the latter coincides with the "velocity frame". In particular, we define

$$\hat{U}_V = \begin{pmatrix} \cos\psi & -\sin\psi & 0 \\ \sin\psi & \cos\psi & 0 \\ 0 & 0 & 1 \end{pmatrix} \begin{pmatrix} \cos\gamma & 0 & -\sin\gamma \\ 0 & 1 & 0 \\ \sin\gamma & 0 & \cos\gamma \end{pmatrix} \begin{pmatrix} 1 & 0 & 0 \\ 0 & \cos\phi & \sin\phi \\ 0 & -\sin\phi & \cos\phi \end{pmatrix} \tag{5.4}$$

$$= \begin{pmatrix} \cos\gamma\cos\psi & -\cos\phi\sin\psi + \sin\phi\sin\gamma\cos\psi & -\sin\phi\sin\psi - \cos\phi\sin\gamma\cos\psi \\ \cos\gamma\sin\psi & \cos\phi\cos\psi + \sin\phi\sin\gamma\sin\psi & \sin\phi\cos\psi - \cos\phi\sin\gamma\sin\psi \\ \sin\gamma & -\sin\phi\cos\gamma & \cos\phi\cos\gamma \end{pmatrix}, \tag{5.5}$$

where ψ is the velocity yaw (heading angle), γ the velocity pitch (flight-path angle), and ϕ the roll (banking angle). Observe that $\hat{x}_V = \hat{U}_V\hat{x}$, $\hat{y}_V = \hat{U}_V\hat{y}$, and $\hat{h}_V = \hat{U}_V\hat{h}$.

Before we continue, it is worth pointing out that the orientation of our coordinate systems deviates from the convention in flight mechanics. Often the x, y, and z-axis are interpreted as north, east, and downwards, respectively, hence one defines the altitude then as $h = -z$, see, e.g., Beeler, Moerder, and Cox (2003) and Hull (2007). We prefer to work with x, y, and h only, which results into a different rotation matrix $\hat{U}_V$.

Flight with the absence of wind

Let us assume our glider experiences no moving atmosphere. In the three dimensional setting, a standard form for the equations of motion

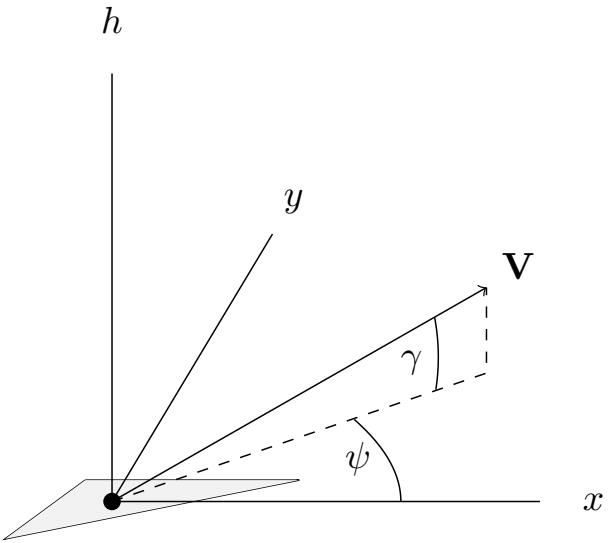

Figure 5.6: A three-dimensional sketch of the ground axes frame. Note that the banking angle ϕ is the only angle not being depicted in the diagram; this particular angle depends on how much the plane is rolling about the airspeed vector $\mathbf{V}$.

for a point mass glider is

$$\dot{V} = -\frac{D}{m} - g\sin\gamma \tag{5.6}$$

$$\dot{\gamma} = \frac{L\cos\phi}{mV} - \frac{g}{V}\cos\gamma \tag{5.7}$$

$$\dot{\psi} = \frac{L\sin\phi}{mV\cos\gamma} \tag{5.8}$$

$$\dot{x} = V\cos\psi\cos\gamma \tag{5.9}$$

$$\dot{y} = V\sin\psi\cos\gamma \tag{5.10}$$

$$\dot{h} = V\sin\gamma. \tag{5.11}$$

Equations (5.6)–(5.8) are the so-called dynamics equations. The kinematic equations for the velocity vector $\mathbf{V} = \begin{pmatrix} \dot{x} & \dot{y} & \dot{h} \end{pmatrix}$ are given by (5.9)–(5.11). Relatively more advanced equations of motion, taking either side or thrust forces into account as well, can be found in Beeler, Moerder, and Cox (2003) and Hull (2007), respectively.

Remark 4. Observe that in the equations above, the banking angle ϕ is presumed to be a control parameter (which may be time dependent). Usually, in the study of flight mechanics, this is a feasible presumption, because a pilot is able to adjust this angle by simply adjusting the wing flaps of the airplane.

It is clear that we cannot control this as easily in our application. Nevertheless, observe that the changes in $\phi = \phi(t)$ are caused by the paddle only and that $\phi = 0$ holds when the paddle is absent. In particular, under additional assumptions, we are able to relate the banking angle ϕ with the angles made by the paddle, see Subsections 5.2.3 and 5.2.3. Alternatively, one is able to obtain an approximation of ϕ by looking at the data (see recommendations and outlook). Different model assumptions, such as saying that ϕ is proportional to $\dot{\psi}$ at an earlier time instant (hence, a delay differential equation), are thought to be possible and numerically tractable.

So, from now we just assume that—indeed—we are able to control the angle ϕ.

A derivation of the equations of motion above can be found in Weitz (2015). Although elementary, we show its derivation for the sake of completeness and because the several observations made are useful for the flight model with wind. By recalling Figure 5.5, we see that the resultant external force becomes

$$\mathbf{F} = \mathbf{L} + \mathbf{D} + \mathbf{G} \tag{5.12}$$

$$= [-D - mg\sin\gamma]\hat{x}_V + mg\cos\gamma\sin\phi\hat{y}_V + [L - mg\cos\gamma\cos\phi]\hat{h}_V. \tag{5.13}$$

On the other hand, since $\mathbf{V} = V\hat{x}_V$ holds, we obtain that the acceleration relative to the ground is given by

$$\mathbf{a} = \frac{d\mathbf{V}}{dt} = \dot{V}\hat{x}_V + V\frac{d\hat{x}_V}{dt}. \tag{5.14}$$

Expressing the time derivative of $\hat{x}_V$ within the coordinates of the rotating reference frame, gives us

$$\frac{d\hat{x}_V}{dt} = -[\dot{\gamma}\sin\phi - \dot{\psi}\cos\gamma\cos\phi]\hat{y}_V + [\dot{\gamma}\cos\phi + \dot{\psi}\cos\gamma\sin\phi]\hat{h}_V. \quad (5.15)$$

This relationship is easily verified; a direct calculation uses the angular velocities and invokes the transport theorem, see, e.g., Weitz (2015). Substituting equation (5.15) in equation (5.14) yields

$$\mathbf{a} = \dot{V}\hat{x}_V - V[\dot{\gamma}\sin\phi - \dot{\psi}\cos\gamma\cos\phi]\hat{y}_V + V[\dot{\gamma}\cos\phi + \dot{\psi}\cos\gamma\sin\phi]\hat{h}_V. \quad (5.16)$$

Using the second law of Newton, equation (5.13), and equation (5.16), we get the following dynamics equations:

$$m\dot{V} = -D - mg\sin\gamma, \quad (5.17)$$

$$mV[\dot{\gamma}\sin\phi - \dot{\psi}\cos\gamma\cos\phi] = -mg\cos\gamma\sin\phi, \quad (5.18)$$

$$mV[\dot{\gamma}\cos\phi + \dot{\psi}\cos\gamma\sin\phi] = L - mg\cos\gamma\cos\phi. \quad (5.19)$$

It is obvious (5.17) is equivalent to (5.6). The following observation is extremely useful: we are able to decouple the other two equations in such ways that we will get the first order differential equations (5.7) and (5.8).

When we multiply equation (5.18) by $\sin\phi$ and equation (5.19) by $\cos\phi$ and add the resulting two expressions, we obtain

$$mV\dot{\gamma} = L\cos\phi - mg\cos\gamma. \quad (5.20)$$

Similarly, when we multiply equation (5.18) by $\cos\phi$ and equation (5.19) by $\sin\phi$ and subtract the resulting two expressions from one another, we find

$$mV\cos\gamma\dot{\psi} = L\sin\phi. \quad (5.21)$$

This motivates the equations of motion (5.6)–(5.11).

Flight with the presence of wind

For the two dimensional setting, we refer to Chapter 2 of Hull (2007) for an analogous model to the one below (with thrust) which includes

a comprehensive derivation as well. In line with their approach, we derive our three dimensional model. Also, note the similarities with Weitz (2015), yet we will follow slightly different assumptions.

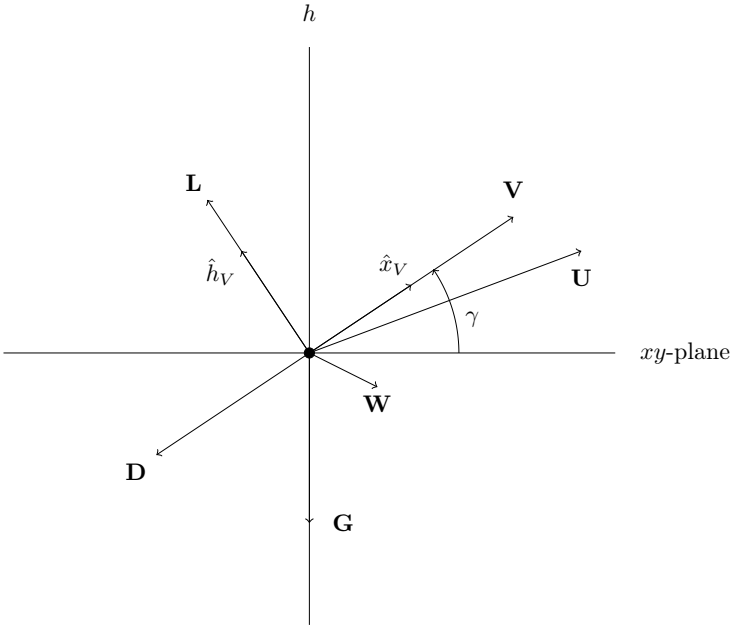

Figure 5.7: A force diagram in the case of a moving atmosphere **W**.

By writing $\mathbf{W} = (W_x, W_y, W_z)^T$, we notice that the kinematic equations become

$$\dot{x} = V \cos\gamma \cos\psi + W_x \tag{5.22}$$

$$\dot{y} = V \cos\gamma \sin\psi + W_y \tag{5.23}$$

$$\dot{z} = V \sin\gamma + W_z. \tag{5.24}$$

In the scenario where the wind velocity is constant, the dynamic equations (5.6)–(5.8) do not change. In other words, the equations of motion of the glider are then given by the coupled differential equations (5.6)–(5.8) together with (5.22)–(5.24).

Nevertheless, given that the wind field $\mathbf{W}$ changes over time (which is the case for our application), we need to consider the time derivative of $\mathbf{W}$ into the dynamics equations. The acceleration relative to the ground is given by

$$\mathbf{a} = \frac{d\mathbf{U}}{dt} = \frac{d\mathbf{V}}{dt} + \frac{d\mathbf{W}}{dt} = \frac{d\mathbf{V}}{dt} + (\dot{W}_x, \dot{W}_y, \dot{W}_z)^T. \tag{5.25}$$

As before, we would like to express $\mathbf{a}$ in terms of the wind axes frame (now a moving atmosphere is present). Recall that

$$\frac{d\mathbf{V}}{dt} = \dot{V}\hat{x}_V - V[\dot{\gamma}\sin\phi - \dot{\psi}\cos\gamma\cos\phi]\hat{y}_V + V[\dot{\gamma}\cos\phi + \dot{\psi}\cos\gamma\sin\phi]\hat{h}_V. \tag{5.26}$$

Consequently, in the wind axes frame we have

$$\begin{aligned}
\mathbf{a} &= \frac{d\mathbf{V}}{dt} + \hat{U}_V(\dot{W}_x, \dot{W}_y, \dot{W}_z)^T && (5.27)\\
&= \big(\dot{V} + \dot{W}_x\cos\gamma\cos\psi + \dot{W}_y\cos\gamma\sin\psi + \dot{W}_z\sin\gamma\big)\hat{x}_V + \\
&\quad \big(-V[\dot{\gamma}\sin\phi - \dot{\psi}\cos\gamma\cos\phi] + \dot{W}_x\hat{U}_{21} + \dot{W}_y\hat{U}_{22} + \dot{W}_z\hat{U}_{23}\big)\hat{y}_V + && (5.28)\\
&\quad \big(V[\dot{\gamma}\cos\phi + \dot{\psi}\cos\gamma\sin\phi] + \dot{W}_x\hat{U}_{31} + \dot{W}_y\hat{U}_{32} + \dot{W}_z\hat{U}_{33}\big)\hat{z}_V,
\end{aligned}$$

where $\hat{U}_{ij} := (\hat{U}_V)_{ij}$. Once again, using the second law of Newton, equation (5.13), and equation (5.28), we get the following dynamics equations:

$$m\dot{V} = -D - mg\sin\gamma + \tag{5.29}$$

$$- m\left(\dot{W}_x\cos\gamma\cos\psi + \dot{W}_y\cos\gamma\sin\psi + \dot{W}_z\sin\gamma\right), \tag{5.30}$$

$$mV[\dot{\gamma}\sin\phi - \dot{\psi}\cos\gamma\cos\phi] = -mg\cos\gamma\sin\phi + m\left(\dot{W}_x\hat{U}_{21} + \dot{W}_y\hat{U}_{22} + \dot{W}_z\hat{U}_{23}\right), \tag{5.31}$$

$$mV[\dot{\gamma}\cos\phi + \dot{\psi}\cos\gamma\sin\phi] = L - mg\cos\gamma\cos\phi - m\left(\dot{W}_x\hat{U}_{31} + \dot{W}_y\hat{U}_{32} + \dot{W}_z\hat{U}_{33}\right). \tag{5.32}$$

Decoupling equations (5.31) and (5.32) as before, results into the dy-

namics equations:

$$\dot{V} = -\frac{D}{m} - g\sin\gamma - \dot{W}_x\cos\gamma\cos\psi - \dot{W}_y\cos\gamma\sin\psi - \dot{W}_z\sin\gamma \tag{5.33}$$

$$\dot{\gamma} = \frac{L\cos\phi}{mV} - \frac{g}{V}\cos\gamma + \frac{1}{V}\big(\dot{W}_x\sin\gamma\cos\psi + \dot{W}_y\sin\gamma\sin\psi - \dot{W}_z\cos\gamma\big) \tag{5.34}$$

$$\dot{\psi} = \frac{L\sin\phi}{mV\cos\gamma} + \frac{1}{V\cos\gamma}\big(\dot{W}_x\sin\psi - \dot{W}_y\cos\psi\big). \tag{5.35}$$

In conclusion, the equations of motion of the glider with a general wind field is given by

$$\dot{V} = -\frac{D}{m} - g\sin\gamma - \dot{W}_x\cos\gamma\cos\psi - \dot{W}_y\cos\gamma\sin\psi - \dot{W}_z\sin\gamma \tag{5.36}$$

$$\dot{\gamma} = \frac{L\cos\phi}{mV} - \frac{g}{V}\cos\gamma + \frac{1}{V}\big(\dot{W}_x\sin\gamma\cos\psi + \dot{W}_y\sin\gamma\sin\psi - \dot{W}_z\cos\gamma\big) \tag{5.37}$$

$$\dot{\psi} = \frac{L\sin\phi}{mV\cos\gamma} + \frac{1}{V\cos\gamma}\big(\dot{W}_x\sin\psi - \dot{W}_y\cos\psi\big). \tag{5.38}$$

$$\dot{x} = V\cos\psi\cos\gamma + W_x \tag{5.39}$$

$$\dot{y} = V\sin\psi\cos\gamma + W_y \tag{5.40}$$

$$\dot{h} = V\sin\gamma + W_z, \tag{5.41}$$

where we recall

$$L = \frac{1}{2}\rho V^2 S C_L \quad \text{and} \quad D = \frac{1}{2}\rho V^2 S C_D, \tag{5.42}$$

Apart from different angles orientations, a major difference between the model above compared to the model in Weitz (2015) is that we do not assume the wind direction is in the xy-plane. For our intents and purposes, we require W_z and $\dot{W}_z$. Additionally, one usually assumes that W_x, W_y, and W_z are functions of t, x, y, and h, and computes the time derivatives with the chain rule, see also Hull (2007). We will not do this, since W_x, W_y, W_z and their time derivatives are supposed to be obtained from the data or/and by means of computational fluid dynamics simulations (see recommendations and outlook).

5.2.3 A simplified flight model

The model in the previous section is useful for doing detailed simulations on the glider when coupled to a computational fluid dynamics simulator of the airflow generated by the paddle. In this section, however, we take an alternative approach by simplifying the models above. These can then be used to approximate several quantities like the glide angle and the turning radius. This section can be read independently from the section above.

Flying straight ahead

Firstly, we look at the case where the glider flies straight, so that the y-component can be ignored. Like earlier, we let $\mathbf{U} = (U_x, U_z)$ denote the velocity of the glider with respect to the ground and $\mathbf{W} = (W_x, W_z)$ the velocity of the wind generated by the paddle. The relative airspeed of the glider with respect to the wind is given by $\mathbf{V} = \mathbf{U} - \mathbf{W}$. The angle of the vector $\mathbf{V}$ relative to the ground (i.e., with the x-axis), which we denote with γ, is given by

$$\arctan\left(\frac{V_z}{V_x}\right). \tag{5.43}$$

The total aerodynamic force acting on the glider is a combination of the drag D in the opposite direction of $\mathbf{V}$ and the lift L perpendicular to $\mathbf{V}$. By introducing the unit vectors $e_{\mathbf{V}} = (\cos\gamma, \sin\gamma)$ and $e_{\perp\mathbf{V}} = (-\sin\gamma, \cos\gamma)$, we can mathematically express the above as

$$\mathbf{F}_{aero} = Le_{\perp\mathbf{V}} - De_{\mathbf{V}} = \frac{1}{2}\rho V^2 S(C_L e_{\perp\mathbf{V}} - C_D e_{\mathbf{V}}). \tag{5.44}$$

where $V = \|\mathbf{V}\|$. For the lift and drag coefficients, C_L and C_D, we use a standard formulation like in Beeler, Moerder, and Cox (2003):

$$C_D = C_{D_0} + \varepsilon C_L^2, \quad C_L = C_{L_\alpha}\alpha, \tag{5.45}$$

where

$$\varepsilon = \frac{1}{\pi ARe}, \quad C_{L_\alpha} = \frac{\pi AR}{1 + \sqrt{1 + (AR/2)^2}}. \tag{5.46}$$

Note that these equations are only valid for a small angle of attack $\alpha = \chi - \gamma$, i.e., the angle between the pitch angle of the wing χ and the airspeed vector $\mathbf{V}$. Subsequently, taking the aerodynamic force $\mathbf{F}_{aero}$ and the gravity, $\mathbf{F}_g = -mge_z$, into account results into the following set of equations of motion:

$$\dot{U}_x = -\frac{1}{2m}\rho V^2 S(C_L \sin\gamma + C_D \cos\gamma), \tag{5.47}$$

$$\dot{U}_z = -g + \frac{1}{2m}\rho V^2 S(C_L \cos\gamma - C_D \sin\gamma), \tag{5.48}$$

$$\dot{x} = U_x, \tag{5.49}$$

$$\dot{z} = U_z. \tag{5.50}$$

The equations above can be made more explicit by observing that $V^2 = (U_x - W_x)^2 + (U_z - W_z)^2$ holds, which reduces to $V^2 = U_x^2 + U_z^2$ in absence of the paddle.

For these equations we will now analytically investigate the equilibrium situation $\dot{U}_x = \dot{U}_z = 0$. In words, we solve for a flight trajectory with constant velocity. Notice that setting $\dot{U}_x = 0$ yields the equality

$$C_L \sin\gamma + C_D \cos\gamma = C_{L_\alpha}(\chi-\gamma)\sin\gamma + (C_{D_0} + \varepsilon C_{L_\alpha}^2(\chi-\gamma)^2)\cos\gamma = 0, \tag{5.51}$$

which we can solve for γ. Using $\chi \approx 0$ as the value for the pitch angle and applying the small angle formulae $\sin\gamma \approx \gamma$ and $\cos\gamma \approx 1$ gives us the following approximation for γ at equilibrium:

$$\gamma_{\text{eq}} \approx -\sqrt{\frac{C_{D_0}}{C_{L_\alpha} - C_{L_\alpha}^2 \varepsilon}}. \tag{5.52}$$

The minus sign is due to the fact that $\mathbf{V}$ is pointing downwards. Consequently, setting $\dot{U}_z = 0$ gives us a value for the airspeed at equilibrium, namely

$$V_{\text{eq}} = \sqrt{\frac{2mg}{\rho S(C_L \cos\gamma_{\text{eq}} - C_D \sin\gamma_{\text{eq}})}}. \tag{5.53}$$

Using the values in Table 5.1, we find

$$\gamma_{\text{eq}} \approx -5.5^\circ \quad \text{and} \quad V_{\text{eq}} \approx 0.75\,\text{m/s}. \tag{5.54}$$

Note that these values hold regardless of the wind field $\mathbf{W}$, as long as the wind field is not accelerating. In the scenario where wind is absent, γ is the glide angle and V the velocity of the glider. This implies that without the paddle—and assuming that the glider is not going to accelerate—the glider falls down with an approximate speed of 0.75 m/s and under an angle of 5.5°. In particular, we can decompose V_{eq} as

$$V_{x,\text{eq}} \approx 0.74\,\text{m/s} \quad \text{and} \quad V_{z,\text{eq}} \approx 0.07\,\text{m/s}. \tag{5.55}$$

This equilibrium is, in fact, stable (which is easily verified with standard techniques). If we simulate the equations of motion (5.47)–(5.50) without wind (see Figure 5.8), we see that the glider's angle and velocity converge to the found values in (5.54) and (5.55).

A simplified wind model

A full treatment of the airflow induced by the paddle requires a quite complex computational fluid dynamics (CFD) simulation, like in Figure 5.9 from Sweden International Physicist's Tournament (2017). To circumvent this heavy machinery, we introduce some simplifications, enabling us to do some elementary calculations.

1. We assume that we can perfectly match the speed of the paddle with the horizontal speed of the glider U_x and we keep it at a fixed angle θ and a fixed height above the ground.

2. We assume that we can see the airflow as two dimensional, so it only has a component in the x and z direction.

3. We model only the airflow above the boundary layer, a small region where the friction with the paddle has a large effect.

4. In the co-moving frame of reference of the paddle, there is an incoming horizontal airflow with speed U_x. We assume that the paddle only deflects the airflow and that the speed of the airflow is conserved.

5. We assume that at the edge of the boundary the airflow is parallel with the paddle and that the vertical component decays expo-

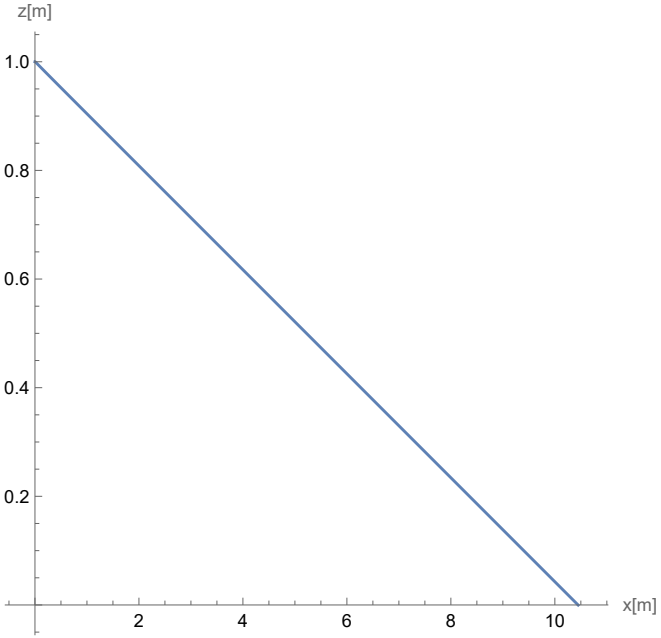

Figure 5.8: A simulation of the equations of motion (5.47)–(5.50) with values of Table 5.1 and initial conditions $x = 0\,\mathrm{m}, z = 1\,\mathrm{m}, U_x = 0.75\,\mathrm{m/s}, U_z = 0\,\mathrm{m/s}$. Observe that the solution quickly converges to the equilibrium state; see equations (5.54) and (5.55).

nentially with a factor c_w and the perpendicular distance to the paddle.

Now, let z denote the height above the boundary layer and consider the perpendicular distance to the paddle given by $\frac{z}{\cos\theta}$. To transform back to the ground reference frame, we are required to add the velocity of the paddle $(U_x, 0)$. With the assumptions above, we use the following equation to model the wind from the ground perspective:

$$\mathbf{W}(U_x, z, \theta) = U_x(1 - \sqrt{1 - e^{-\frac{2c_w z}{\cos\theta}} \sin^2\theta}, e^{-\frac{c_w z}{\cos\theta}} \sin\theta). \qquad (5.56)$$

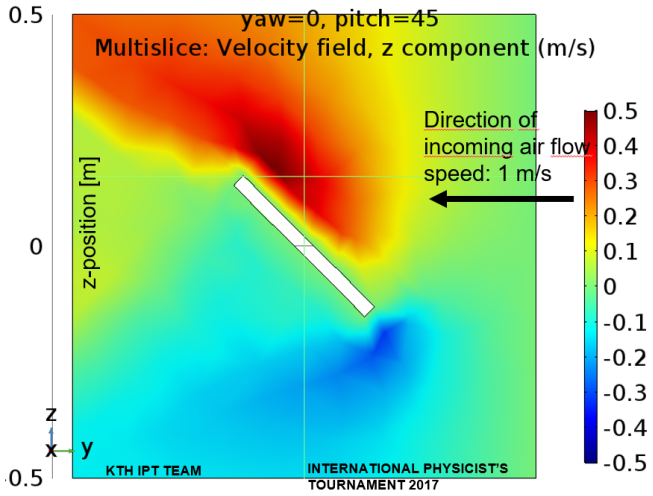

Figure 5.9: A CFD simulation of the airflow induced by the paddle from Sweden International Physicist's Tournament (2017).

Remark 5. The model in (5.56) is an ad hoc description and simplication of the wind generated by the paddle. We have chosen this specific formulation, but we would like to emphasise that we do not exclude other possibilities. This particular choice for the wind field also enabled us to obtain nice closed forms for U_x and z, see (5.58) and (5.59).

Remark 6. Assuming that the wind direction is two dimensional, the paddle length is effectively infinite. For a relatively small paddle, this assumption could be problematic. Moreover, we do not treat the boundary layer, as we assume that the glider is unable to fly here, so it does not need to be modelled. The exponential decay $e^{-\frac{c_w z}{\cos\theta}}$ matches the properties observed from the CFD simulations (Figure 5.9): for $z = 0$ this factor is 1, for $z \to \infty$ it vanishes, and the gradient of the speed difference is proportional with the distance. Ultimately, the choice $\frac{z}{\cos\theta}$, instead of, e.g., $z\cos\theta$, was to better reflect the fact that the wind velocity substantially decreases as θ increases.

We can now use the values of constant flight of the previous subsection, i.e.,

$$\gamma_{\text{eq}} = -5.5^\circ \quad \text{and} \quad V_{\text{eq}} = 0.75\,\text{m/s}, \tag{5.57}$$

to solve for the case where the glider keeps its altitude, i.e., $U_z = 0$. From the equation $\mathbf{V} = \mathbf{U} - \mathbf{W}$ and the wind model description (5.56), we deduce

$$U_x = V_{\text{eq}} \quad \text{and} \quad \sin(-\gamma_{\text{eq}}) = e^{-\frac{c_w z}{\cos\theta}} \sin\theta. \tag{5.58}$$

Using that the height is postive, i.e., $z > 0$, we obtain $\theta > -\gamma_{\text{eq}} = 5.5^\circ$. By analysing Figure 5.9, we estimate $c_w \approx 3\,\text{m}^{-1}$. An estimation for c_w suffices, since it only defines the length scale of z. We can solve for the height of z:

$$z = -\frac{\cos\theta}{c_w} \log\left(\frac{\sin(-\gamma_{\text{eq}})}{\sin\theta}\right). \tag{5.59}$$

We can plot the height z as a function of the paddle angle θ, see Figure 5.10.

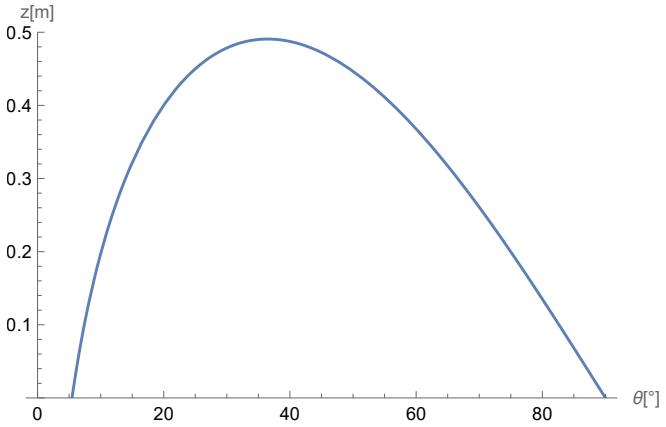

Figure 5.10: The height above the paddle z for a glider with constant speed (5.59) as a function of the paddle angle θ with the parameters $c_w = 3\,\text{m}^{-1}$ and $\gamma_{\text{eq}} = -5.5^\circ$.

The optimal paddle angle is when the stable height above the paddle z is maximal. In this case if there is a disturbance in the airflow, there

is more space to recover before the glider enters the turbulent boundary layer and is unable to fly.

Differentiating the function in (5.59) and setting it equal to zero, we find that for $\gamma_{\text{eq}} = -5.5°$ the optimal angle is $\theta = 36°$. For different glider angles see Figure 5.11.

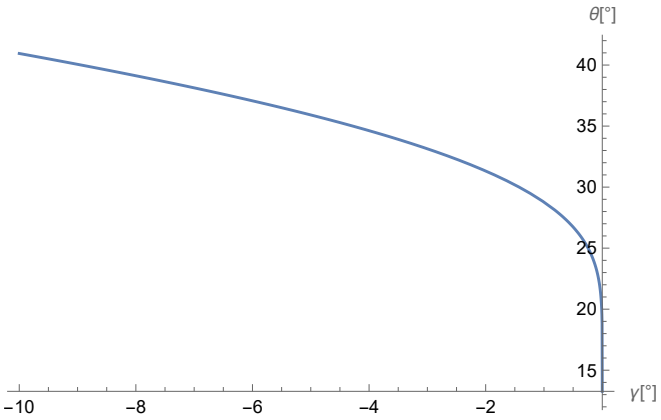

Figure 5.11: For each $\gamma = \gamma_{\text{eq}}$, we plot the optimal paddle angle θ, i.e., the paddle angle for which the function in equation (5.59) is maximal.

Turning radius of the glider

We can make the glider turn by just rotating the paddle. Indeed, rotating the paddle causes a difference in the airflow at each wing, initiating a different lift force on each wing, see Figure 5.12. The imbalance in lift induces a torque on the glider, which makes the glider bank.

To compute the turning radius, we assume that the glider is flying a perfect circle of radius R with constant speed U_x. In this section we consider the vehicle reference frame to be our coordinate system, so we write x for the tangential direction of the circular trajectory—positive in the direction of movement—and write y for the radial direction—positive in the inward direction for a left turn. For uniform circular

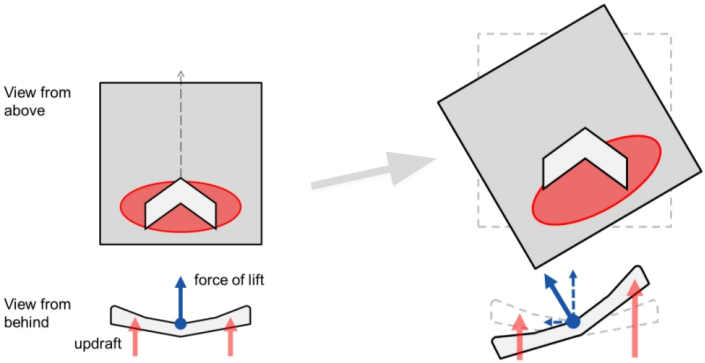

Figure 5.12: The effect of rotating the paddle below the glider. The red spot illustrated on the paddle is often referred to as the sweet spot. This figure is a modified version of a figure in Sweden International Physicist's Tournament (2017).

motion, we need the centripetal force of the glider to be equal to

$$F_c = \frac{mU_x^2}{R}. \tag{5.60}$$

Denote the banking angle by ϕ, which is positive if the right wing tips up. Now, we can decompose the aerodynamic force along the z-direction of the coordinate system used in (5.47)–(5.50), where we have $\phi = 0$, into a upwards, z-direction, and a sidewards, y-direction, pointing vector. For a left turn with constant speed and radius, we can derive the equations of motion by equating the forces in the x, z and y direction, respectively:

$$\tfrac{1}{2}\rho V^2 S(C_L \sin\gamma + C_D \cos\gamma)\cos\phi = 0 \tag{5.61}$$

$$\tfrac{1}{2}\rho V^2 S(C_L \cos\gamma - C_D \sin\gamma)\cos\phi = mg \tag{5.62}$$

$$\tfrac{1}{2}\rho V^2 S(C_L \cos\gamma - C_D \sin\gamma)\sin\phi = \frac{mU_x^2}{R}, \tag{5.63}$$

where $V = \|\mathbf{V}\|$. The first equation gives us (5.51), where we had found $\gamma_{\text{eq}} \approx -5.5°$. Equation (5.62) yields a solution for V, which we will denote by $V_{\text{eq},c}$, where

$$V_{\text{eq,c}} = \sqrt{\frac{2mg}{\rho S(C_L \cos\gamma_{\text{eq}} - C_D \sin\gamma_{\text{eq}})\cos\phi}} = \frac{V_{\text{eq}}}{\sqrt{\cos\phi}}. \tag{5.64}$$

By using the wind model (5.56), we can set $U_x = V_{\text{eq,c}}$ (similar as before), and solving the last equation (5.63) results into the closed form

$$R = \frac{2m}{\rho S(C_L \cos\gamma_{\text{eq}} - C_D \sin\gamma_{\text{eq}})\sin\phi}. \tag{5.65}$$

We have plotted $V_{\text{eq,c}}$ and R against the banking angle ϕ in Figure 5.13. For $\phi = 30°$, we find that $V_{\text{eq,c}} \approx 0.78\,\text{m/s}$ and $R \approx 17\,\text{cm}$ holds.

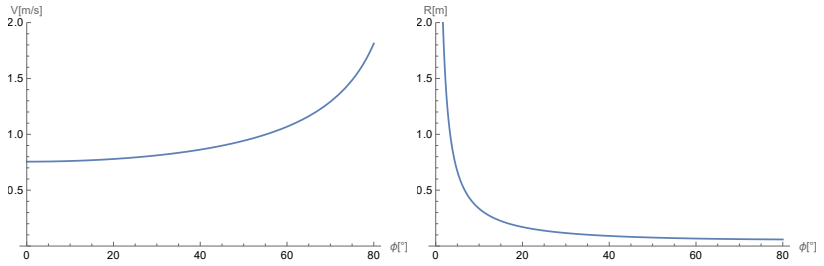

Figure 5.13: The relative speed $V_{\text{eq,c}}$, see (5.64), and turning radius R, see (5.65), plotted against the banking angle ϕ. The glider then moves in a perfect circular trajectory, assuming that the wind generated by the paddle can be approximated with the function in equation (5.56).

Increasing the banking angle with the paddle

As mentioned previously, we can model the aerodynamic force on each on the wings individually. We denote the airflow at the left wing by W_{left} and at the right wing by W_{right}, which consequently induces a force on the left wing $F_{\text{aero,left}}$ and a force on the right wing $F_{\text{aero,right}}$. For this section we only consider the force in the upwards direction

with respect to the ground. When this force on the left and right wing is unequal, the induced torque makes the glider bank. This torque is the difference between the forces on the left and right wing multiplied by the arm d. Recall, the arm is the distance between the centerline of the glider and the point on the wing where the force acts, which we approximate as $b/4$. The second derivative of ϕ is then given by the torque divided by the moment of inertia. We approximate the latter as $\frac{1}{12}mb^2$, resulting into the equation

$$\ddot{\phi} = \frac{3}{mb}(F_{\text{left}} - F_{\text{right}}). \tag{5.66}$$

Our goal is to model the change in airflow W due to turning the paddle by an angle ξ. The factor in (5.56) which is the most significant, right now, is the height z. By turning the paddle we increase the height of the left wing and decrease the height of the right wing. With some trigonometric computations, we find that this increase/decrease is equal to $d \sin\xi \sin\theta$. On the other hand, when the banking angle ϕ increases and the plane banks to the right, we find the height decreases on the right wing and increases on the left wing. This increase/decrease is equal to $d \sin\phi$. These two effects cancel out when $\sin\xi \sin\theta = \sin\phi$, which means that $W_{left} = W_{right}$ and the torque is zero. Combining this relation with (5.65) connects the angle turning angle of the glider to the turning radius of the paddle. Mathematically put, we obtain

$$R \sin\xi \sin\theta = \frac{2m}{\rho S(C_L \cos\gamma_{\text{eq}} - C_D \sin\gamma_{\text{eq}})} = constant. \tag{5.67}$$

5.3 Data-driven approach

In parallel to the model-driven approach described in Section 5.2, we used the video data recorded by Zoro Feigl as a starting point of this problem. We begin by discussing the contents of these videos. We then describe our methods for generating data based on the videos and conclude with an analysis of the obtained data.

5.3.1 Available data

Several videos were available of Zoro Feigl flying the walkalong glider in his workplace. In these videos, the camera is mounted behind the paddle. The panel is transparent, allowing for a view of the glider in a consistent perspective. Moreover, the bottom of the glider is marked with a cross consisting of a line from the top to the bottom of the glider in its center and a line from the left wing to the right wing. A characteristic frame from one of the videos is shown in Figure 5.14.

Figure 5.14: Frame of one of the available videos in which Zoro Feigl flies the walkalong glider.

In the videos we observed that the pitch of the glider does not vary much throughout the flight. Hence, we have made the assumption that the pitch of the plane is constant ($\chi = 0$). To extract useful information from the videos, the first step is to detect and locate the glider. This problem is challenging due to a few factors at play.

First, at some points in the videos there is significant background light, which makes it difficult, even for humans, to locate the cross on the glider exactly. Moreover, the perspective of the camera varies between videos and is not completely consistent even within one video. This complicates relating the measurements from these videos to the world coordinate system. Furthermore, the trajectory of the paddle is unknown, which makes relating the data to movements made with the

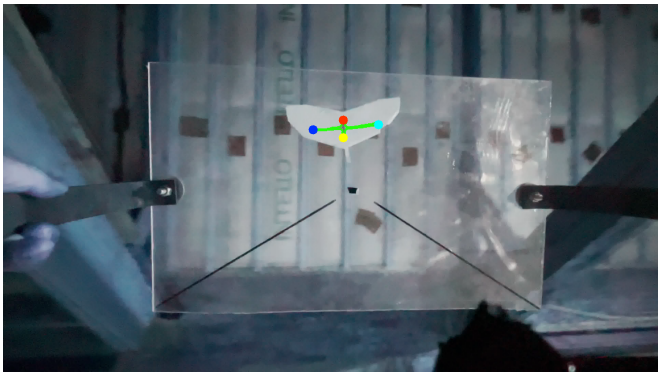

Figure 5.15: Tracking of the cross on the glider by image processing.

paddle impossible. Lastly some relevant factors, as discussed in the modeling section, for example the distance between the glider and the paddle, are challenging to acquire from 2D video data from a single viewpoint.

5.3.2 Detecting the glider

In order to detect the glider in the video footage, we used two methods. First, we implemented an image processing procedure to detect the plane. Subsequently, we implemented a deep learning algorithm in order to make the tracking more robust against variations in lighting and environment.

Classic image processing

Based on the frames as shown in Figure 5.14, we detected the white glider and the cross on the glider, which gave us a location of the 4 points on all ends of the cross (Figure 5.15).

However, this detection is far from perfect, as changes in light/background may result in failures, making the measurements that we obtain with this method very noisy and imperfect.

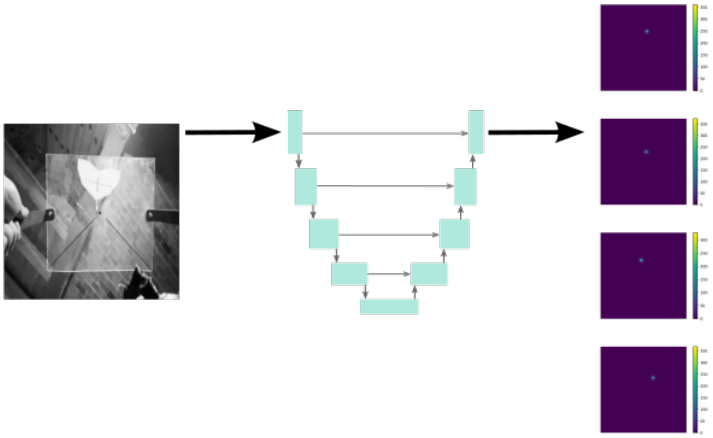

Figure 5.16: Deep learning approach for estimating the location of the glider. Resampled frame is used as input for a CNN, predicting four 2D functions indicating the location of the vertices of the cross drawn on the glider.

Deep learning approach

As we identified in the classic imaging approach, the automatic detection of the plane is not robust against changes in lighting and background. Over the last number of years, convolutional neural networks (CNN's) have become very popular in common imaging processing tasks, such as classification, detection and segmentation. CNN's handle image data by extracting distinctive features using consecutive convolution operations. The weights of the convolution kernels and hence the features they pick up are based on the data and follow from an extensive optimization process we refer to as training. It has been well-established that CNN's can be trained to become invariant to these type of conditions, by means of proper data augmentation Shorten and Khoshgoftaar (2019). This means that the automatic detection system can be deployed in a wide variety of surroundings.

To train our network, we first need proper ground-truth data. For

this, we manually annotated the four vertices of the cross in a number of frames of one video. The CNN should predict the locations of these four vertices based on image data. To solve this image detection problem, we adapt the method introduced in Sironi et al. (2015), that casts this as a regression problem. For each vertex, we construct a 2D function indicating the location of the vertex with a Gaussian peak, as shown on the right of Figure 5.16. The CNN that we use maps the 2D input image to four 2D output images, predicting the function value for each of their respective vertices, also shown in Figure 5.16. To retrieve the location of each vertex in the image frame, we can simply take the argmax of each of the four images.

We trained a U-Net architecture on a small dataset consisting of 30 samples. The frames from the original video had a resolution of 3840×2160 and had three colour channels. As a preprocessing step, we first resampled the frames to 256×256 pixels, and reduced the colour channels to gray values. These resampled input images are shown on the left of Figure 5.16. We trained the network for 1000 epochs, using an Adam optimizer with a mean squared error loss with learning rate 0.001.

We tested this method on unseen frames, similar to the ones with ground truth annotations. A resulting prediction on one of these frames is shown in Figure 5.17a. The maxima of the predicted locations align with the actual locations of the cross. We only annotated slices at the beginning of the video, due to time constraints in this project [10]. Therefore, for new and unseen situations, the network shows a poor performance (Figure 5.17b). In this case, the glider angle and background lighting differ a lot from the data used for optimization, the network struggles to detect the vertices on the glider. Since detecting the glider on familiar scenes looks promising, we recommend using more annotations with more variety in background and lighting, as well as orientation of the glider as training data for the network.

[10] Annotating the cross on additional video data is not extremely labour intensive.

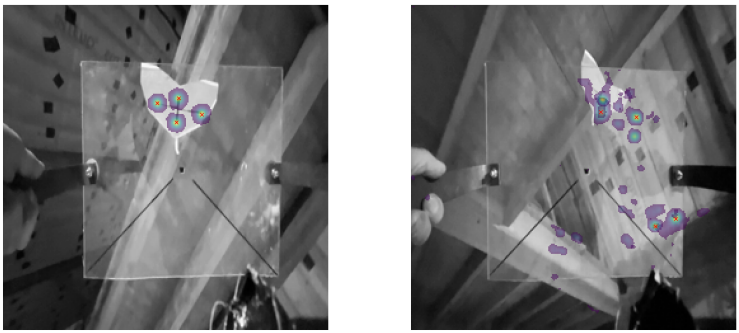

(a) Unseen, similar frame (b) Unseen, non-similar frame

Figure 5.17: Vertex locations determined using the trained network on different frames of the video.

5.3.3 Analysis of obtained data

We now analyse the data as obtained using the classic image processing approach. As the four points of the cross drawn on the glider are detected, it is possible to find the center point of the cross under the assumption that the paper does not bend. This can then be done by taking the intersection of the line between the leftmost and rightmost point and the line between the top point and bottom point. We then plot the distribution of the measured center points as a heatmap, shown in Figure 5.18. Note that badly detected crosses, identified by a small difference between coordinates of the four points, are not included in the heatmap.

In this heatmap, we see that the glider's position remains close to a specific position relative to the camera. This suggests that it is beneficial for control of the glider to also keep the glider relatively constant in respect to a camera mounted on the robot. Further analysis of videos in which the glider falls could give more insight into the feasibility of certain positions.

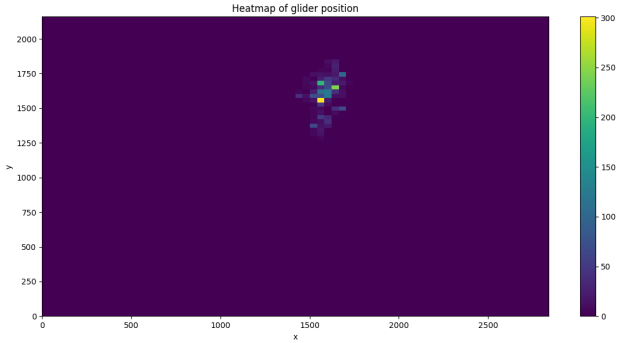

Figure 5.18: Heatmap of the center of the glider relative to the camera. Colours represent the number of frames the center of the glider was in that location in the image frame.

Next, we attempt to find the yaw of the glider. To do this, we assume that the pitch and roll relative to the board are constant, and we thus take the yaw to be the angle of the observed vertical line of the cross. This angle is taken so that an angle of 0 rad corresponds to a vertical line. A positive angle corresponds to the plane turning right and a negative angle corresponds to the plane turning left (Figure 5.19).

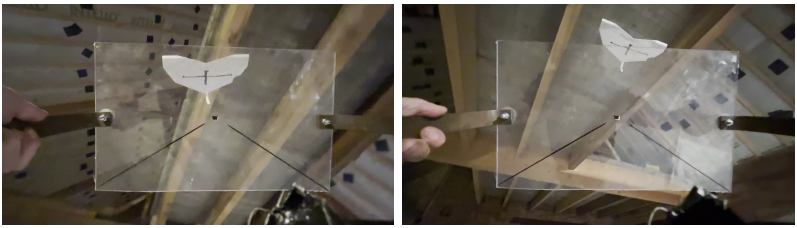

Figure 5.19: Examples of frames for which a small negative yaw (left) and a positive yaw (right) are detected.

Measuring the angle of the plane as observed through the screen for one of the videos provided, we find the result shown in Figure 5.20.

When viewing the video next to this data, large spikes in the observed yaw seemed to correspond to the plane turning in various instances. Therefore, our notion based on these results was that measuring the yaw while flying the glider could help in determining whether controlled actions of the robot have the desired effect. Particularly, it could be used as an indication of whether the glider is turning at a desired rate.

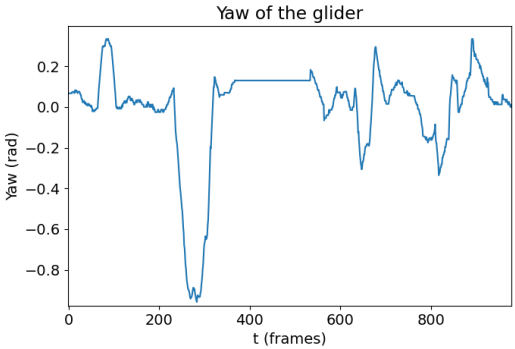

Figure 5.20: Plot of the estimated yaw over time.

5.4 Recommendations and outlook

Based on our findings, we have several recommendations for further development of a control system for the glider project.

From our analysis of the position of the glider, we observed the position of the center of the glider relative to the board is very stable in the correctly scored frames. We expect this could be used as an indication for a control algorithm, as the glider straying too far from the "stable" state could indicate that the control is not working as intended. Moreover, imprecise comparisons between the measured yaw of the glider relative to the board and the corresponding video seem to indicate that a change in yaw correlates with the plane making a turn. This is an observation that can be taken into account when constructing

a control strategy. Lastly, the results of our deep learning approach for locating the glider are promising, though more time and data are needed to properly train this network. We expect that such a deep learning approach is appropriate for locating the glider and finetuning control parameters based on processed data on-the-fly.

Large improvements to the data-driven methodologies can be obtained if more details of the data are collected. If the location and distance relative to the camera of all four points of the cross on the glider are known, the metrics discussed in this report could be measured and analysed in much more detail. This leads to more insight in the stable position and rotation of the glider both while turning and flying straight. Finally, we have noticed that the image processing methods applied in this report tend to fail in case of high contrast within the background, or heavy backlight in the video data. This indicates that the room where the installation is placed can influence the effectiveness of control strategies that are based on real-time collected data. Therefore, testing the installation relatively long before the exhibition is opened to visitors is recommended as then changes to either the room or parameters in the control strategy can still be made.

Note that enhancing the data-driven models as proposed above significantly improves the practicality of the model-driven part already. In particular, when we predict the trajectory of the glider, we require a lot of information that should be retrieved from the data. For a proper prediction we need the live location of the glider, as well as its speed and its velocity yaw and pitch. Retrieving the banking angle from the data would be very useful as well, but when the glider is forced to move in a perfect circle, this angle can simply be determined by the angles made by the paddle (see Subsections 5.2.3 and 5.2.3). We think that the banking angle can be retrieved by clever markings on the glider. Also, due to the fact that the location of the paddle is always known—thanks to the technology of the robot arm—we recommend a setup that is able to measure all the angles and distances between the glider and the paddle. This information is just essential for prediction.

Furthermore, we advise those who continue with this project to investigate whether our (simplified) models are realistic. Especially, in the simplified model we approximate the wind generated by the paddle instead of using CFD simulations in order to win computation time,

but perhaps this simplification does not coincide with experiments and thus it needs to be verified. Doing more numerical analyses may yield more insight in the flight dynamics of the glider as well. In particular, we expect that several parameters in the models can be quite sensitive. For example, slight changes in the mass parameter m may result into very different results, since the mass of the glider is relatively small (see Table 5.1) and we divide by m in the models. In addition, we do not expect that all the constants in Table 5.1 are correct; these constants can be found by doing enough experiments and subsequently data fitting.

We also recommend—from a modelling perspective—to start with one of the following "simple" trajectories: 1) an almost-circle, i.e., a circular trajectory where the glider needs to fly partly in a straight line without a paddle underneath for a short while (which is due to the fact the robot arm is unable to move in circles indefinitely); 2) an eight-like figure, where the intersection point is above the robot arm. Option 1 is favourable, because then one can use the simplified models. Note that the glider can fly a long distance straight ahead without upward lifting. Option 2 is a favourable trajectory in the sense that it would then not be necessary to let the glider leave the paddle at all. How often one needs to do small corrections and subsequently predict the glider's trajectory again, is something to look into. We actually expect predictions will hold for quite a long time in a proper environment, but there is no problem with regularly applying corrections (if computation time allows it).

Ultimately, a useful continuation of this project may include the construction of a control algorithm. This control algorithm can at least partly be based on the models and observations presented in this report. One idea would be to use funnel control Hackl, Endisch, and Schroder (2008). This particular type of control does not rely on precise knowledge of the underlying system, and aims to limit the solution of the system to a decaying limiting function in time.

References

Beeler, Scott C, Daniel D Moerder, and David E Cox (2003). *A flight dynamics model for a small glider in ambient winds*. Tech. rep. National Aeronautics and Space Administration (NASA).

Etkin, Bernard (2005). *Dynamics of Atmospheric Flight*. Courier Corporation.

FANUC Benelux BV (2022). *Robot arm, M-710iC/12L*. URL `https://www.fanuc.eu/be/en/robots/robot-filter-page/m-710-series/m-710ic-12l`, last accessed on February 17, 2022.

Feigl, Zoro (2021). *Spooky action spatial sketch*. URL `https://www.youtube.com/watch?v=BKchk4GLtQc&ab_channel=ZoroFeigl`, last accessed on March 10, 2022.

Grant, Joseph E (1955). *Method of flying toy airplane and means therefor*. US Patent 2,718,092.

Hackl, Christoph M, Christian Endisch, and D Schroder (2008). "Funnel-control in robotics: An introduction". In: *2008 16th Mediterranean Conference on Control and Automation*. IEEE, pp. 913–919.

Harrison SciencetoyMaker, Slater (2022). *Make the Baby Bug Walkalong Glider*. URL `https://sciencetoymaker.org/walkalong-glider-airsurf-air-surfing/make-your-own-gliders/baby-bug/`, last accessed on February 17, 2022.

Hull, David G (2007). *Fundamentals of airplane flight mechanics*. Vol. 19. Springer.

Shorten, Connor and Taghi M Khoshgoftaar (2019). "A survey on image data augmentation for deep learning". In: *Journal of Big Data* 6.1, pp. 1–48.

Sironi, Amos et al. (2015). "Multiscale centerline detection". In: *IEEE Transactions on Pattern Analysis and Machine Intelligence* 38.7, pp. 1327–1341.

Stengel, Robert F (2004). *Flight Dynamics*. Princeton University Press.

Sweden International Physicist's Tournament, KTH Royal Institute of Technology (2017). *Handy glider*.

Weitz, Lesley A (2015). *Derivation of a point-mass aircraft model used for fast-time simulation*. Tech. rep. MITRE Corporation.